Journal of Applied Fluid Mechanics, Vol. 12, No. 4, pp. 1249-1263, 2019.
Available online at www.jafmonline.net, ISSN 1735-3572, EISSN 1735-3645.
DOI: 10.29252/jafm.12.04.29593

2-D Simulation with OH* Kinetics of a Single-Cycle Pulse Detonation Engine

E. C. Maciel[1] and C. S. T. Marques[1,2†]

[1] *Technological Institute of Aeronautics, São José dos Campos, SP, 12228-900, Brazil*
[2] *Aerothermodynamics and Hypersonics Division, Institute for Advanced Studies, São José dos Campos, SP, 12228-001, Brazil*

†*Corresponding Author Email: tafuri@uol.com.br*

(Received September 2, 2018; accepted December 7, 2018)

ABSTRACT

Two-dimensional computational fluid dynamics (CFD) simulation with selected kinetics for H_2–air mixture of a hydrogen-fuelled single-pulse detonation engine were performed through ANSYS FLUENT commercial software for diagnostic purposes. The results were compared with Chapman–Jouguet (CJ) values calculated by the CEA (Chemical Equilibrium with Applications) and ZND (Zel'dovich–Neumann–Döring) codes. The CJ velocities and pressures, as the product velocities are in agreement, however, the CJ temperatures are too higher for 2-D simulations; as a consequence, the sound velocities were overpredicted. OH* kinetics added to the reaction set allowed visualization of the propagation front with several detonation cells showing a consistent multi-headed detonation propagating in the whole tube. The detonation front was slightly perturbed at the end of the tube with inclination of front edge and fewer cell numbers, and more significantly at the nozzle entrance with velocity reduction, resulting in a weak and unstable detonation. OH* images showed the detonation reaction zone decoupled from the shock front with disappearance of cellular structure. The inclusion of OH* reaction set for CFD simulation coupled to kinetics is demonstrated to be an excellent tool to follow the detonation propagation behaviour.

Keywords: Computational fluid dynamics; Pulse detonation engine; OH* kinetics; OH* images; Diagnostics.

NOMENCLATURE

a	sound velocity
h_i	enthalpy of ith chemical specie
k	turbulent kinetic energy
M	Mach number
M_i	molecular weight of ith chemical specie
p	pressure
T	temperature
u	propagation velocity in the direction of flow
$\vec{v}$	velocity vector
Y_i	mass fraction of ith chemical specie
ρ	density
μ	viscosity

1. INTRODUCTION

Detonation propagation by computational fluid dynamics (CFD) has been studied for many decades (Fickett and Davis, 2010; Lee, 2008). In function of the computational power growth and advances in the numerical methods associated with scientific advances of the experimental investigation on detonation in the 80s and 90s, it was established that the detonation is an option for propulsion (Perkins and Sung, 2005; Kailasanath, and Schawer 2017) with higher performance and fuel economy, due to its higher thermodynamic cycle efficiency.

Detonation is an extremely efficient way of inflammable mixtures burning because of the better driving from chemical energy content and, hence, detonation device manufacture has been pursued by several research groups (Tangirala *et al.*, 2003), in spite of the difficulties in achieving controlled and consistent detonations with suitable frequencies to the detonation cycle (Perkins and Sung, 2005; Tangirala *et al.*, 2003; Kailasanath, 2000).

Pulse detonation engines (PDEs) are one of the

advanced combustion devices with high potential for aerospace propulsion applications; further to their thermodynamic efficiency advantages and mechanical simplicity, they are scalable, reliable and of low cost (Wu *et al.*, 2003). PDEs could be applied single-handedly or coupled to turbo-machines by combining cycles, improving the performance and operational limits of both (Stoddard *et al.*, 2011).

The PDE cycle consists in the filling of the combustion chamber; detonation initiation; wave propagation and products expansion; gases exhaustion where an under-pressure in the detonation tube is generated; purge assisted with high velocity of the exhaust gases and new injection of the air–fuel mixture (Wolański, 2013).

Hydrogen-fuelled PDEs are of great interest, since the first works on these devices (Nicholls *et al.*, 1957), due to the hydrogen properties as low molecular weight, high reactivity, high specific heat, wide combustible limits that lead to higher performances. Furthermore, the use of hydrogen as a substitute fuel to the current petrol fuels has been widely considered because of the pollutant reduction, mainly CO_2 and particulate carbonaceous matter, in spite of its transport, distribution and storage difficulties. Numerical and experimental studies of hydrogen-fuelled PDEs have verified high levels of NOx, but viable techniques for its reduction have been proposed (Wolański, 2013; Yungster *et al.*, 2006; Bozhenkov *et al.*, 2003).

Multidimensional and high-precision CFD simulations, in which the compressibility effect and time evolution of propagation dynamics coupled to the combustion chemistry, are fundamental for better understanding of the operational and performance issues for these detonation engines, in addition to the pollutant production (Kailasanath, and Schwer, 2017; Yungster *et al.*, 2006). These particular characteristics that require a high level of computational mesh refinement in the detonation front and its neighbourhood (Yi *et al.*, 2017) in association with hydrogen chemical kinetics and the inverse dependence of the reaction rates on pressure (Smirnov and Nikitin, 2014) , make it a hard task to simulate hydrogen-fuelled PDEs. Small reaction sets are not able to predict a wide range of combustion conditions and a complete or detailed reaction mechanism adds more complexity to the simulation and computational time consumption. Furthermore, there are phases of detonation phenomena, as detonation initiation and deflagration-to-detonation propagation that are little known. However, the high cost involved in experimental combustor tests and the need of a short time for their development have stimulated the scientific community to apply CFD for prediction and optimization of the PDEs' operational parameters and performance (Anetor *et al.*, 2012; Kim *et al.*, 2003). Therefore, several non-commercial and commercial codes (CFD++, KIVA, SPARK, ANSYS Fluent, etc.) with different numerical methods (finite-difference methods, finite-volume discretization method, weighted essentially non-oscillatory (WENO) discretization scheme) coupled to the skeletal, reduced and detailed chemical kinetics, and also the turbulence models have been employed for this type of study (Perkins and Sung, 2005; Tangirala *et al.*, 2003; Rudy *et al.*, 2014; Gavrikov *et al.*, 2000; Taylor *et al.*, 2013; Zhang *et al.*, 2016; Debnath and Pandey, 2017; He and Karagozian, 2006; Liu *et al.*, 2016).

For simplicity of CFD simulation, several studies have applied direct detonation initiation and a single reaction step (Im and Yu, 2003). However, skeletal kinetic models are not able appropriately to simulate ignition delay times and detonation cellular structure; both parameters allow a good representation of a reaction mechanism (Liu *et al.*, 2016).

CFD has also been employed for detonation and PDE simulations to validate reaction mechanisms and optical diagnostics (Smirnov and Nikitin, 2014; Ebrahimi and Merke, 2002; Mével *et al.*, 2014, 2015; Gallier *et al.*, 2017). The verification and validation of the computational results, in other words, the evaluation of the applied simulation procedures and prediction ability of the applied methods, respectively, are essential for CFD analysis credibility (Mehta, 1998). Therefore, a well-established numerical model could be a complementary tool for experimental optical diagnostics (Mével *et al.*, 2014; Gallier *et al.*, 2017; Pitgen *et al.*, 2003) adding higher quantitative precision for imaging.

As a means to establish a numerical model for supporting the experimental diagnostics of an ideal PDE, 2-D CFD simulations coupled to a reduced reaction mechanism with OH* chemical kinetics by applying ANSYS Fluent 17.0 software were carried out. OH* kinetics permits more accuracy to the multidimensional simulation, enabling and improving the optical diagnostics.

2. NUMERICAL METHODOLOGY

Multidimensional CFD from compressive reactive Reynolds Averaged Navier–Stokes (RANS) equations with k–ε renormalization group (RNG) turbulence model coupled to a reduced chemical kinetics for H_2–air were applied for solution of the detonation wave in an ideal PDE, as described below.

2.1 Governing Equations

Conservation of mass for each chemical species (i):

$$\frac{\partial(\rho Y_i)}{\partial t} + \nabla.(\rho \vec{v} Y_i) = -\nabla.\vec{J}_i + R_i \qquad (1)$$

where is the chemical production rate for the i-th chemical species and $\vec{J}_i$ is the diffusion flow, defined as

$$\vec{J}_i = -\left(\rho D_{i,m} + \frac{\mu_t}{Sc_t}\right)\nabla Y_i - D_{T,i}\frac{\nabla T}{T} \qquad (2)$$

where $D_{i,m}$ and $D_{T,i}$ are mass and thermal diffusion coefficients, respectively, and the turbulent Schmidt

number, $Sc_t = \frac{\mu_t}{\rho D_t}$, where μ_t is the turbulent viscosity and D_t is the turbulent diffusion.

Conservation of momentum:

$$\frac{\partial \rho}{\partial t} + \nabla.(\rho \vec{v}) + \nabla.(\rho \vec{v}\vec{v}) + -\nabla p + \nabla.(\bar{\bar{\tau}}) + \rho \vec{g} + \vec{F} \quad (3)$$

where p is the static pressure, $\rho \vec{g}$ represent the gravitational forces and $\vec{F}$ the external forces.

$\bar{\bar{\tau}}$, the stress tensor, is expressed as follows

$$\bar{\bar{\tau}} = \mu \left[(\nabla \vec{v} + \nabla \vec{v}^T) - \frac{2}{3} \nabla . \vec{v} I \right] \quad (4)$$

where μ is the molecular viscosity, I is the unit tensor; the second term on the right-hand side of the equation represents the volumetric dilatation effect.

Conservation of energy:

$$\frac{\partial}{\partial t}(\rho E) + \nabla.(\vec{v}(\rho E + p)) = \nabla.\left(k_{eff} \nabla T - \sum_i h_i J_i + (\bar{\bar{\tau}}_{ef} . \vec{v}) \right) + S_h \quad (5)$$

where k_{eff} is the effective thermal conductivity and the S_h term includes the energy source from chemical reactions, as follows

$$k_{eff} = k_t + k \quad (6)$$

$$S_{h,r} = -\sum_i \frac{h_i^0}{M_i} R_i \quad (7)$$

where k_t is turbulent thermal conductivity the h_i^0 is the formation enthalpy of each species i.

2.2 Turbulence Model

The RNG k–ε model was used as the turbulence model for hydrogen-fuelled PDE simulation. The model equations are shown in Eqs. (8) and (9).

$$\frac{\partial}{\partial t}(\rho k) + \frac{\partial}{\partial x_i}(\rho k u_i) = \frac{\partial}{\partial x_j}\left(\alpha_k \mu_{eff} \frac{\partial k}{\partial x_j} \right) + G_k + G_b - \rho \varepsilon - Y_M + S_k \quad (8)$$

$$\frac{\partial}{\partial t}(\rho \varepsilon) + \frac{\partial}{\partial x_i}(\rho \varepsilon u_i) = \frac{\partial}{\partial x_j}\left(\alpha_\varepsilon \mu_{eff} \frac{\partial \varepsilon}{\partial x_j} \right) + C_{1\varepsilon} \frac{\varepsilon}{k}(G_k + C_{3\varepsilon} G_b) - C_{2\varepsilon} \rho \frac{\varepsilon^2}{k} - R_\varepsilon + S_\varepsilon \quad (9)$$

where S_k and S_ε are defined by the user; $C_{1\varepsilon}$ and $C_{2\varepsilon}$ are constants equal to 1.42 and 1.68; $C_{3\varepsilon}$ is given by Eq. (10).

$$C_{3\varepsilon} = \tanh \left| \frac{\nu}{u} \right| \quad (10)$$

where ν is the velocity component parallel to the gravity vector and μ is perpendicular component to this vector.

For high Reynolds number, as in detonation, inverse Prandtl effective numbers for k and ε, α_k and α_ε, are equal to 1.393. The additional R_ε term is defined as follows

$$R_\varepsilon = \frac{C_\mu \rho \eta^3 \left(1 - \eta / \eta_0 \right)}{1 + \beta \eta^3} \frac{\varepsilon^2}{k} \quad (11)$$

where $\eta \equiv S_k / \varepsilon$, η_0 = 4.38; β = 0.012 and C_μ = 0.0845.

G_k and G_b represent the generation of turbulent kinetics energy due to the average velocity and fluctuation gradients, respectively, and both are proportional to the turbulent viscosity $(\mu_t = \rho C_\mu \frac{k^2}{\varepsilon})$.

Y_M represents the compressibility effect on turbulence related to the square of the turbulent Mach $(M_t = \sqrt{\frac{k}{a^2}})$ and directly proportional to the rate of dissipation of turbulence energy, ε. The turbulent kinetic energy, k and the rate of dissipation of turbulence energy, ε are calculated through Eqs. (12) and (13).

$$k = \frac{3}{2}(u_{avg} I)^2 \quad (12)$$

$$\varepsilon = C_\mu^{3/4} \frac{k^{3/2}}{l} \quad (13)$$

The term u_{avg} is the average velocity of the flow and I is the turbulence intensity, which is determined by velocity fluctuation and average velocity ratio $(I = \frac{u'}{u_{avg}})$, which determine k. The turbulent length scale, given by l, allows determination of ε.

The RNG k–ε model allows computing the swirl effects from turbulent flows, applying a modified equation for turbulent viscosity, $\mu_{ts} = \mu_t f\left(\alpha_s, \Omega, \frac{k}{\varepsilon}\right)$, where Ω is the swirl number, calculated automatically by the software and α_s is a swirl constant with values dependent on turbulence characteristics affected by swirl (swirl-dominated or middy swirling).

2.3 Chemical Kinetic Models

Chemical reaction kinetics for H_2–air detonation were evaluated through the ZND model, by applying a code from the Explosion Dynamics Laboratory of Caltech (Kao and Shepherd, 2008), with the aim to select the best reduced reaction set for 2-D simulation of an ideal PDE.

Nine reaction mechanisms were tested and compared with a detailed reaction set (Browne *et al.*, 2005) for proper selection. Three reduced chemical kinetics used for high speed deflagration (Zhukov, 2012), DDT (Ivanov *et al.*, 2011) and detonation (Petersen and Hanson, 1999) were not be able to reproduce the results from detailed reaction

Table 1 Reduced reaction chemical kinetics. Reaction rates are presented in the form $k=A\,T^n\,\exp(-E/RT)$ and units are in cm^3, mol, s, K and cal/mol.

Species					
1. H_2		2. H	3. O_2	4. O	5. OH
6. HO_2		7. H_2O_2	8. H_2O	9. N_2	10. OH*
Forward reactions parameters			A	n	*E*
Reaction chemical kinetics from Smirnov and Nikitin (2014)					
1	$H + O_2 = OH + O$		2.00×10^{14}	0.00	16802.0
2	$H_2 + O = H + OH$		5.06×10^{4}	2.70	6285.9
3	$H_2 + OH = H_2O + H$		1.00×10^{8}	1.60	3298.3
4	$OH + OH = H_2O + O$		1.50×10^{9}	1.10	95.6
5	$H + H + M = H_2 + M^*$		1.80×10^{18}	–1.00	0.0
6	$O + O + M = O_2 + M^*$		2.90×10^{17}	–1.00	0.0
7	$H + OH + M = H_2O + M^*$		2.20×10^{22}	–2.00	0.0
8	$H + O_2 + M = HO_2 + M^*$		2.30×10^{18}	–0.80	0.0
9	$H + HO_2 = 2\,OH$		1.50×10^{14}	0.00	1003.8
10	$H + HO_2 = H_2 + O_2$		2.50×10^{13}	0.00	693.1
11	$H + HO_2 = H_2O + O$		3.00×10^{13}	0.00	1720.8
12	$HO_2 + O = OH + O_2$		1.80×10^{13}	0.00	–406.31
13	$HO_2 + OH = H_2O + O_2$		6.00×10^{13}	0.00	0.0
14	$HO_2 + HO_2 = H_2O_2 + O_2$		2.50×10^{11}	0.00	1242.8
15	$OH + OH + M = H_2O_2 + M^*$		3.25×10^{22}	–2.00	0.0
16	$H_2O_2 + H = HO_2 + H_2$		1.70×10^{12}	0.00	3752.4
17	$H_2O_2 + H = H_2O + OH$		1.00×10^{13}	0.00	3585.1
18	$H_2O_2 + O = OH + HO_2$		2.80×10^{13}	0.00	6405.4
19	$H_2O_2 + OH = H_2O + HO_2$		5.40×10^{12}	0.00	1003.8
OH* chemical kinetics from Mével (2009)					
20	$H+O+M = OH^*+M$		6.00×10^{14}	0.00	6940.0
21	$OH^*+H_2O = OH+H_2O$		5.92×10^{12}	0.50	–861.0
22	$OH^*+H = OH+H$		1.50×10^{12}	0.50	0.0
23	$OH^*+H_2 = OH+H_2$		2.95×10^{12}	0.50	–444.0
24	$OH^*+O_2 = OH+O_2$		2.10×10^{12}	0.50	–482.0
25	$OH^*+O = OH+O$		1.50×10^{12}	0.50	0.0
26	$OH^*+OH = OH+OH$		1.50×10^{12}	0.50	0.0
27	$OH^* = OH$		1.46×10^{6}	0.00	0.0

Third-body reactions with M enhanced by $H_2O = 6.5$; $H_2 = 1.0$; $O_2 = 0.4$ and $N_2 = 0.4$.

sets. Another reduced chemical kinetics from Smirnov for H_2–air combustion in engines of different types (based on deflagration, DDT and detonation) (Smirnov and Nikitin, 2014) and a skeletal reactions set (Eklund and Stouffer, 1994), widely applied for supersonic combustion, were also verified without and with OH* kinetics. Further, two OH* reaction sets were simulated (Kathrotia *et al.*, 2010; Mével, 2009).

After careful analysis, the reduced mechanism from Smirnov and OH* kinetics from Mével were selected for PDE simulation (Rodrigues *et al.*, 2015; Maciel, 2017). This reaction set does not include nitrogen chemistry. The insertion of the OH* kinetics gives higher precision to the simulation for comparison with the optical diagnostics results, due to the special characteristics of this radical as a marker of the reaction zone.

Table 1 shows the elementary reactions and their Arrhenius parameters for Smirnov chemical kinetics with Mével's OH* reaction set.

2.4 Equation Discretization

For equation time–space discretization and solution of detonation phenomena in an ideal PDE, the commercial ANSYS Fluent 17.0 was employed, which applies the finite-volume method in each control volume of the computational domain. It uses the Gauss–Seidel method that solves the linear equations system in time together with the Algebraic Multigrid Method (AMG) that solves the linear transport equations from pressure–velocity variables using an implicit method. These methods are coupled to pressure-based solver, which solves simultaneously the system of momentum and pressure-based continuity equations and after updating the mass flux, it solves the energy, species, turbulence and other scalar equations.

For chemical kinetics equations, the solver CFD-CHEMKIN was used with Eddy-Dissipation-Concept (EDC). EDC is a turbulence–chemistry interaction model that assumes small turbulence structures (fine scales) where the reaction occurs.

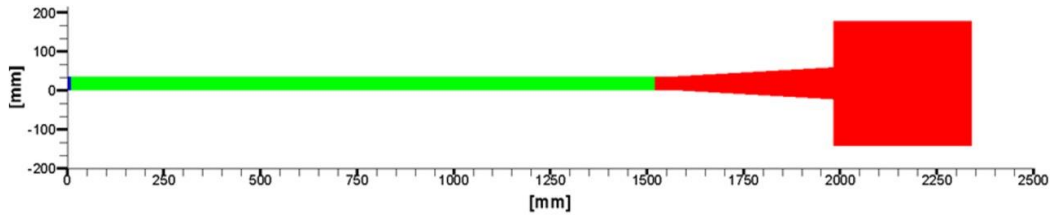

Fig. 1. Computational domain as two regions with different composition and pressure.

The fine structures drive both the dissipation of turbulence energy into heat and the molecular mixing. With detailed chemistry, the fine structures regions are considered as well-stirred reactors and the chemical reactions take place after a specific time scale (Magnussen, 2005). They are important mainly in detonation initiation, when a fast deflagration propagates to become a detonation (Deiterding and Bader, 2005).

Numeric stability and precision are fundamental for reliable results and further for detonation (Navaz and Berg, 1998). Hence, the Courant–Friedrich–Lewy (CFL) number and time step (Δt) must be carefully chosen. As recommended for detonation simulations (Srihari *et al.*, 2015), the CFL number was set as 0.1 to 1 and the maximum time step was adjusted using the equation below

$$\Delta t \leq CFL\left(\frac{\Delta x}{D_{CJ}}\right) \tag{14}$$

where D_{CJ} = 1968.5 m/s (Marques *et al.*, 2010) and Δx is the computational grid spacing.

The upwind second-order space discretization was chosen for energy, density, momentum and chemical species in the cell faces from the grid,

while second-order centred interpolation was selected for pressure. The Green–Gauss node-based the second-order implicit method for transient formulation were applied. The setting of time–space discretization follows the works on H_2–air detonation simulations (Srihari *et al.*, 2015; Taylor *et al.*, 2012, 2013; Sugiyama and Matsuo, 2012).

2.5 Simulation conditions

Figure 1 shows the computational domain for the two-dimensional H_2–air detonation simulation in an ideal PDE, where two regions are considered. It represents the real dimensions of the experimental single-shot pulsed detonation device (Marques *et al.*, 2010).

The first region represents the detonation tube of 36 mm internal diameter (D) and 1520 mm length closed by an ignition flange and a diaphragm, where the H_2–air mixture at 1 atm (101.325 kPa) is placed. The second region is that where the detonation expansion occurs, when the diaphragm is burst and it is under 10 Pa of air. The tube transversal section is constant up to 1580 mm, where a divergent nozzle begins with 6.5º, whose length is 1980 mm. The nozzle is inserted in the test chamber with 320 mm internal diameter and 500 mm length. There is no physical separation barrier of the two regions in the computational model.

In simulations, the initial temperature of 300 K, 21% O_2 and 79% N_2 as air composition, and adiabatic walls were considered. Further, specific heat, thermal conductivity and viscosity were determined by ideal-gas-mixing law from ANSYS Fluent. However, the mass diffusivity for all species considered in the two regions was defined as 2.88 × 10^{-5} m^2/s.

Ignition of stoichiometric H_2–air detonation was provided by a narrow rectangular region of high pressure and temperature with circular regions in front of it, all regions are composed by H_2O, as the Oran research group has applied (Tangirala *et al.*, 2003; Taylor *et al.*, 2012). The detonation ignition is improved by collisions from the shock front produced in the hot and compressed regions (Taylor *et al.*, 2012).

Figure 2 shows the ignition method adopted. CJ detonation initiation at short distance was acquired from a 3 mm × 36 mm region with 500 atm and 4000 K. The pressure and temperature values employed for detonation initiation did not affect the CJ conditions reached after detonation stabilizing. Furthermore, the deposited energy is lower than the critical initiation energy for direct detonation of H_2–air mixtures (Benedick *et al.*, 1986).

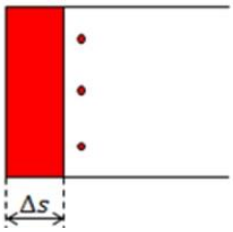

Fig. 2. High pressure and temperature patch with circular regions.

A high refinement level of the detonation front is required for phenomena solution and it is higher as reaction number grows. The grid convergence study showed that CJ velocity values (D_{CJ}) for direct detonation are independent of grid spacing smaller than 100 μm and in these conditions velocities very close to D_{CJ} were found (0.97–1.02 D_{CJ}). In addition, cellular detonation structure was visible for mesh refinement of 50 μm. Therefore, the dynamic refinement from ANSYS Fluent was employed by increasing the cell number, where large density changes occur. A computational grid

Table 2 Propagation parameters for the stoichiometric H_2–air detonation

		P_{VN} (atm)	P_{CJ} (atm)	T_{CJ} (K)	D_{CJ} (m/s)	Mach	Sound Velocity (m/s)	Gas Velocity (m/s)
CEA		-	15.6	2942	1969	1.00	1091	1091
ZND		27.6	15.2	2925	1969	0.99	1125	1115
Smirnov	0.75 m	85.8	13.3	3650	1821	0.75	1340	1005
	1.5 m	101.4	14.0	3650	1996	0.85	1225	1041
Smirnov with OH*	0.75 m	111.5	16.4	3650	1952	0.77	1350	1040
	1.5 m	96.7	13.7	3650	1939	0.83	1275	1058

with spacing of 250 μm with 1.58 million cells, a time step (Δt) equal or less than 1×10^{-7} s and at least 50 μm of refinement (three levels) in the regions (shock front and reaction zone) of large density changes were used.

Operational conditions for a reliable and stable detonation in PDEs are those with ca. 0.9–1.1 D_{CJ}, but it is possible to establish an operational condition in the limit of detonation propagation, where the velocity is 0.85 D_{CJ} (Virot *et al.*, 2009). For this reason, detonation cell widths (λ) were calculated from CELL-H2 (Gavrikov *et al.*, 2000) to parameterize the simulations on the detonation propagation limits. Detonation velocities must be above 1820 m/s (0.92 D_{CJ}) at the end of the detonation tube for reliable and stable propagation, for which detonation cell width is equal to the tube diameter ($\lambda = 36$ mm) and $\lambda = D$ is recognized as a practical criterion for the propagation limit due to the uncertainties on cell sizes near the limit (Thomas, 2009; Dupré *et al.*, 1991). Meanwhile, for CJ detonation, the cell width is 10 mm.

3. RESULTS AND DISCUSSION

3.1 2-D Model Validation

Simulation results for detonation propagation in the tube for both reaction sets from Smirnov without and with OH* chemical kinetics were very similar, as expected.

Figure 3 presents simulated detonation velocity profiles, extracted from longitudinal line of the 2-D plot at the tube centre ($Y = 18$ mm) for each 0.25 m, while Figs. 4 to 6 display the velocity, pressure and temperature 2-D mappings at 1.5 m.

Slight differences, below 10%, could be verified in the simulated CJ detonation parameters with CJ conditions were established at the end of the reaction zones and with this aim the simulated HO_2 profiles found for both the reaction sets were applied. All intermediate species are a majority in the reaction zone, after then there is a quasi-steady state. The OH* radical is an excellent space and time marker of the reaction zone, but was simulated only in one of the reaction sets. CJ detonation velocities (D_{CJ}) were extracted from velocity profiles at the end of the reaction zones in Fig. 3.

Table 2 displays the results calculated by CEA and ZND one-dimensional codes, and those from 2-D CFD coupled to a reduced chemical kinetics scheme.

As shown in Table 2, simulated von Neumann pressures from the two-dimensional model were 3–4 times higher from those calculated by ZND code and were also significantly higher than other 2-D simulations, which also exceed notably those from ZND (He and Karagozian, 2006; Liu *et al.*, 2016). However, the initial high pressure (500 atm) required for detonation initiation led to these results, similarly to 2-D simulations where 200 atm were applied for shock-induced detonation and reflected shocks of about 90 atm for initiation were found (Kim *et al.*, 2003). However, most of the CJ addition of OH* chemical kinetics (Figs. 3 to 6). Simulated detonation velocities showed higher differences, around 0.9–1.10 D_{CJ} from Smirnov and around 0.95–1.20 D_{CJ} from Smirnov with OH* kinetics were found in the whole propagation. However, only in a small region the detonation velocity at the end of tube was outside the 10% change (Fig. 4(b)). Furthermore, simulated velocities from the reaction set with OH* kinetics had lower fluctuations in the detonation front (Fig. 4).

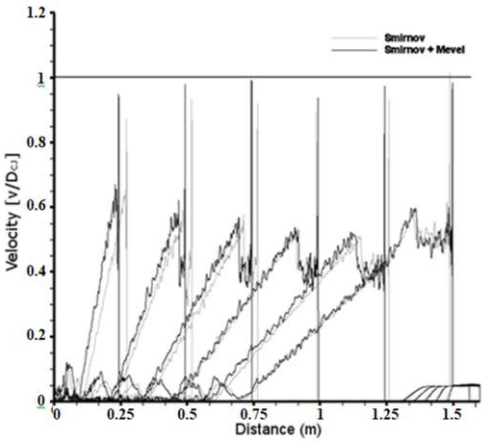

Fig. 3. Simulated H_2-air detonation velocity profiles in the propagation axis.

CJ detonation parameters simulated from 2-D CFD coupled to the chemical kinetics were compared with those calculated through CEA (Marques *et al.*, 2010) and ZND codes for evaluation and validation of the model. They were extracted from plot analysis at 0.75 m and 1.5 m, as in Fig. 7. Von Neumann pressures were also determined from pressure profiles in these plots.

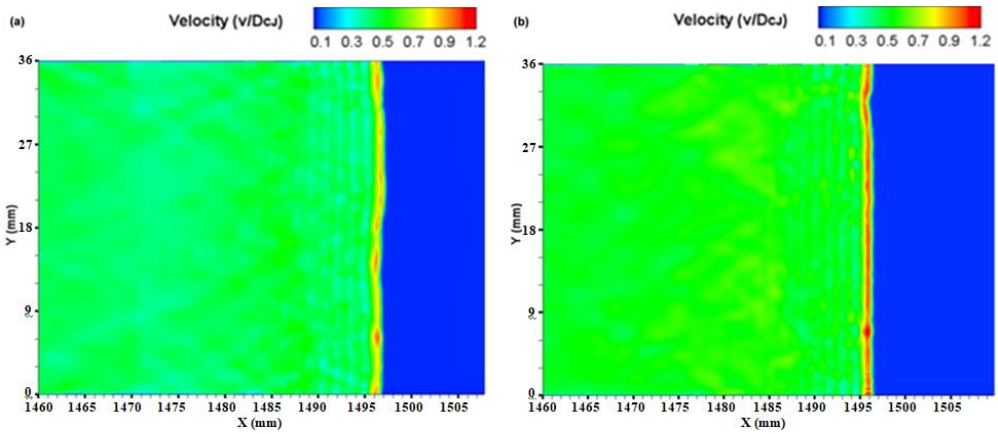

Fig. 4. Velocity mapping at 1.5 m. (a) Smirnov reaction set; (b) Smirnov reaction set with OH* chemical kinetics.

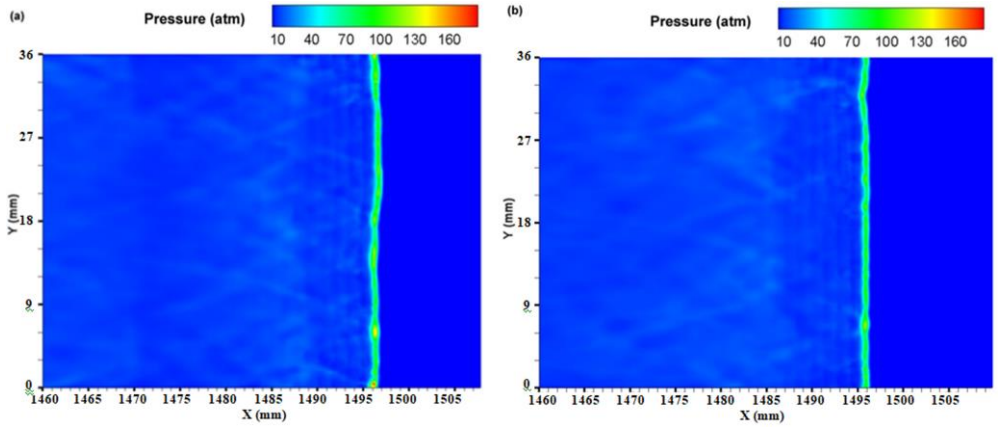

Fig. 5. Pressure mapping at 1.5 m. (a) Smirnov reaction set; (b) Smirnov reaction set with OH* chemical kinetics.

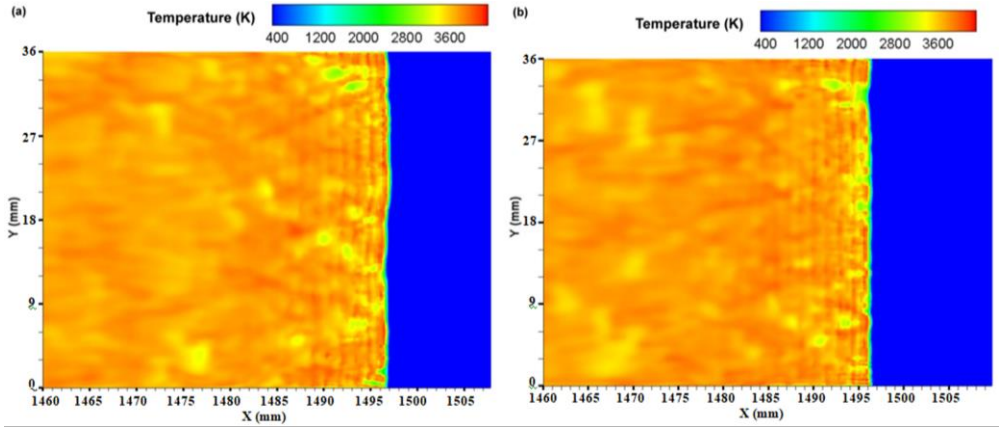

Fig. 6. Temperature mapping at 1.5 m. (a) Smirnov reaction set; (b) Smirnov reaction set with OH* chemical kinetics.

detonation parameters were in good agreement, mainly at the end of the detonation tube. Deviations of ca. 10% for CJ pressures, 1–2% for CJ velocities, 15–17% for Mach, 10–15% for sound velocities and 3–7% for gas velocities were found at the end of the detonation tube. The only exception was the temperature, which was 24% above, because of the high energy deposited for detonation initiation associated with the reaction mechanism and numerical method employed.

As can be observed in Fig. 7, the CJ plane (Mach = 1) was shifted for lower Mach, probably due to the higher sound velocities found, as a consequence of the high simulated CJ temperatures.

Furthermore, 2-D CFD coupled to chemical kinetics

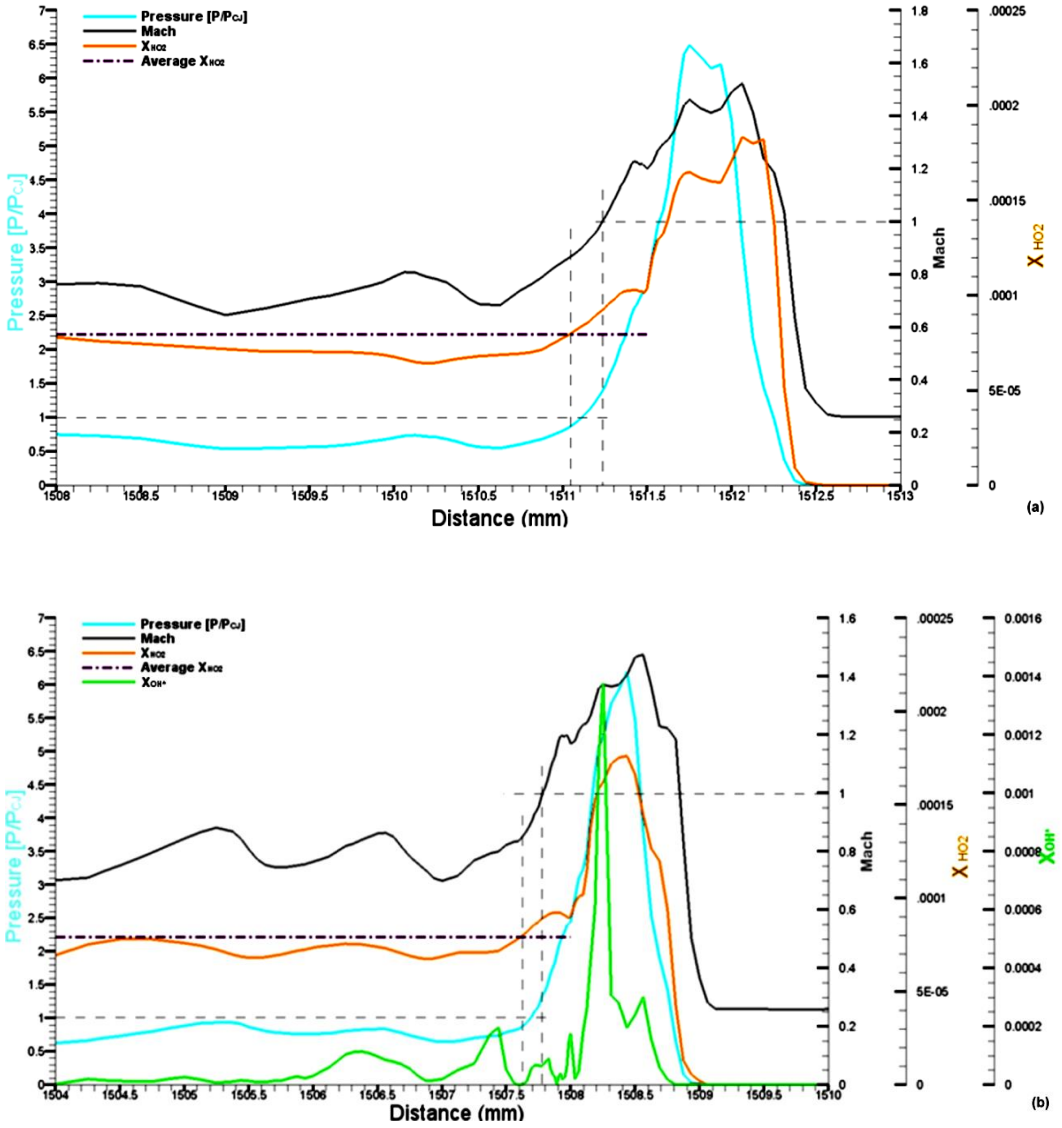

Fig. 7. Pressure, Mach and mole fractions simulated profiles. (a) Smirnov reaction set; (b) Smirnov reaction set with OH* chemical kinetics.

resulted in a cell detonation width of 1 mm. In spite of being higher than the experimental values, these findings are usual for H_2–air detonation (Gamezo *et al.*, 1999) and other 2-D simulations with chemical kinetics had the same results (Taylor *et al.*, 2012, 2013). Simulated reaction and induction zones with thickness around 2 mm and 0.5 mm, respectively, were found. They are lower than those calculated for 1-D steady detonations (Powers and Paolucci, 2005) and similar for multidimensional simulations (Taylor *et al.*, 2013; Im and Yu, 2003).

Therefore, as it is supposed 10–15% fluctuations on CJ conditions for consistent and stable detonation propagation are acceptable and, as well as cellular structure and reaction zone thickness are typically underpredicted by multidimensional simulations with chemical kinetics, 2-D simulations applied in this work can be considered validated for detonation propagation through nozzle.

3.2 Detonation Propagation in the tube by Simulated OH* Images

Detonation propagation behaviour in the tube was also verified by simulated OH* images at each 0.25 m, shown in Figs. 8 to 10.

OH* images demonstrate stable H_2–air multi-headed detonation propagation, in which the detonation front has a height of more than three detonation cells (Boeck *et al.*, 2016). Detonation cells are defined by the shock triple point, where the reaction is very intense and the OH* concentration is high. Simulated OH* images (Figs. 8 to 11) exhibit these multicellular structures, as has been recently experimentally observed (Boeck *et al.*, 2013, 2016; Rankin *et al.*, 2017). Further, the detonation cells verified in OH* images were coincident with the regions of higher heat release simulated, not shown here.

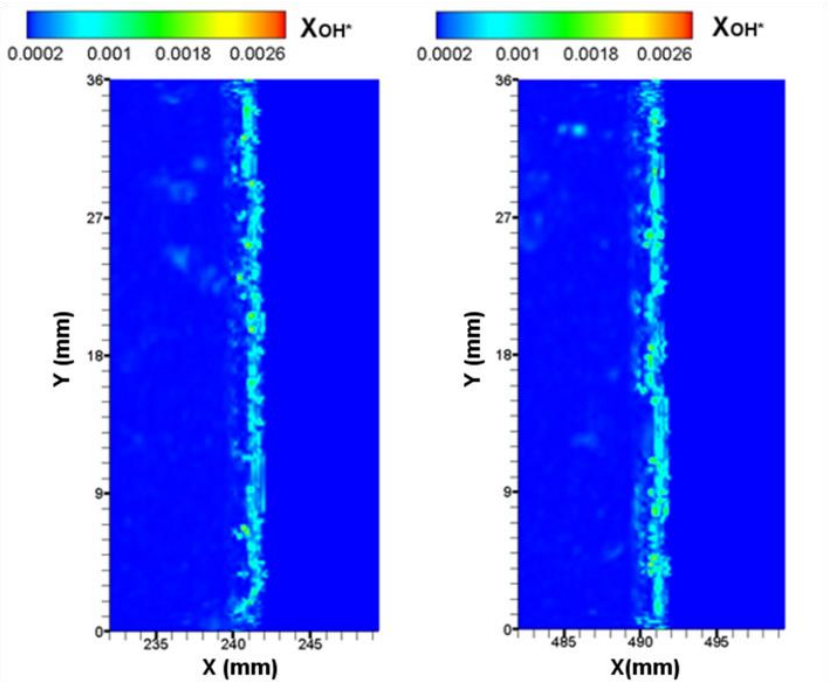

Fig. 8. Simulated OH* images at 0.25 m and 0.50 m in the detonation tube.

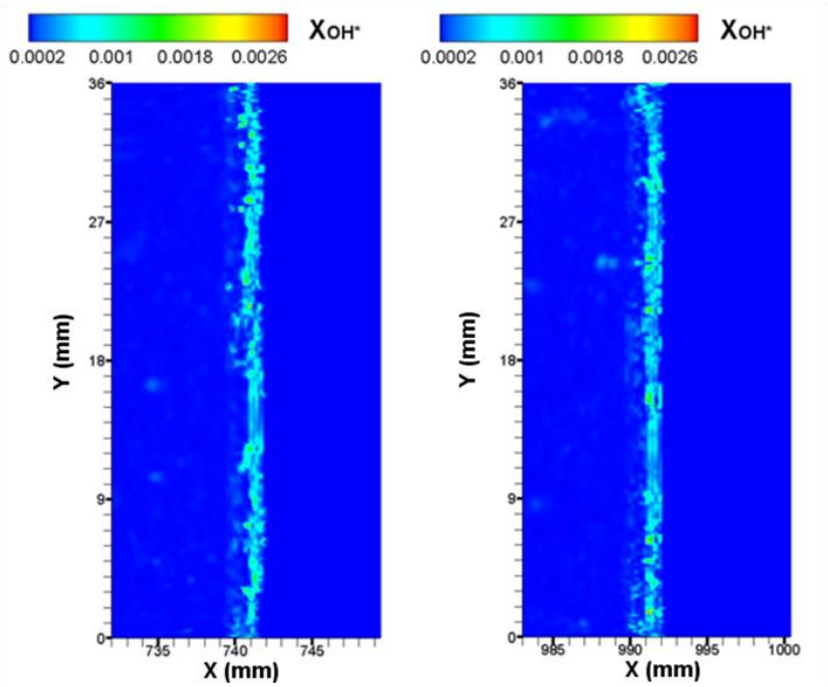

Fig. 9. Simulated OH* images at 0.75 m and 1.00 m in the detonation tube.

From OH* images at 0.25 m, 1.00 m and 1.25, it was possible to verify a slight inclination of detonation fronts near the tube wall and at these positions the detonation velocities were lower (Fig. 3). At 1.25 m, the detonation front seems to be more inclined near the tube bottom wall (Fig. 11), similar experimental OH* images have shown this behaviour for a transition regime (Boeck *et al.*, 2016). In addition, the simulated OH* image at 1.50 m displayed a reduced number of detonation cells compared with those at 1.25 m and the detonation front was straighter. However, the OH* image at the end of the tube did not characterize an unstable propagation regime or a single-head detonation (Boeck *et al.*, 2016). Furthermore, it is supposed to have a dilution effect of the reagents due to the interface of the vacuum region at 10 Pa, where no physical barrier separating it from the fresh mixture was placed in the computational domain.

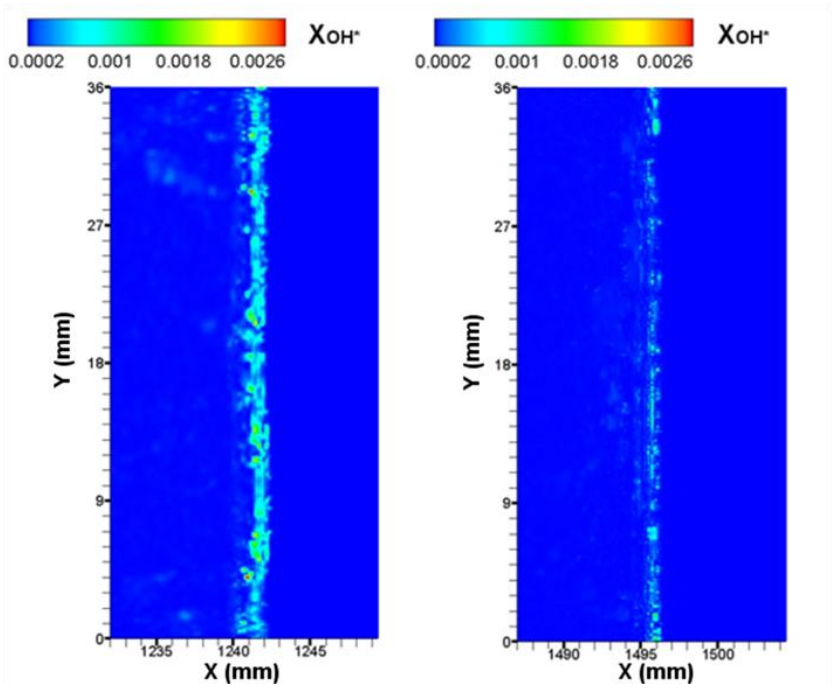

Fig. 10. Simulated OH* images at 1.25 m and 1.50 m in the detonation tube.

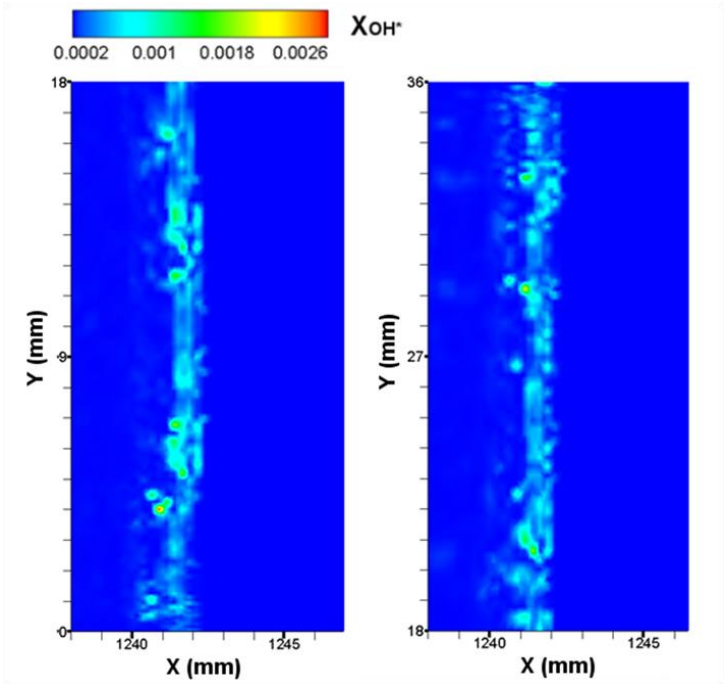

Fig. 11. Simulated OH* images at 1.25 m with expanded scale.

3.3 Detonation Propagation Through Nozzle

Immediately at the beginning of the expansion region, the simulated detonation velocities were reduced and later in the nozzle they were still lower, as shown in Table 3. The lower velocities were accomplished by lower pressures. The detonation velocities were reduced until those (<1674 m/s) typically for a degraded detonation.

The pressure mapping in Fig. 12 at the nozzle exit and OH* image in Fig. 13, both obtained at the same time instant, show clearly that the reaction zone was detached from the shock front. In addition, the reaction zone with cellular structure observed in the OH* images by centres of high reaction intensity disappeared and an extended reaction zone was placed in those thinner thicknesses.

Table 3 Velocities of the detonation propagation through nozzle until products exhaust

Distance (m)	Velocity (m/s)
1.53	1900
1.55	1850
1.58	1750
1.60	1300
1.70	1300
1.85	1425
2.00	1225

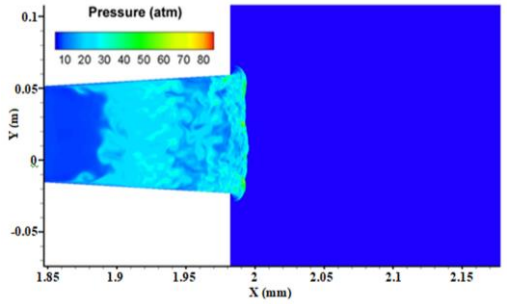

Fig. 12. Pressure mapping at nozzle exit.

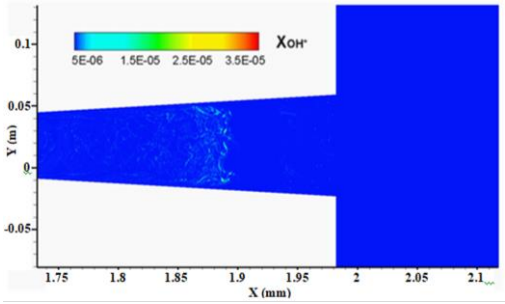

Fig. 13. Simulated OH* image at the same time step of the pressure mapping (Fig. 12).

Figures 14, 15 and 16 display the velocity mapping, the Schlieren and OH* images of the PDE exhaust plume. The Schlieren image was obtained through the first derivative of the density field.

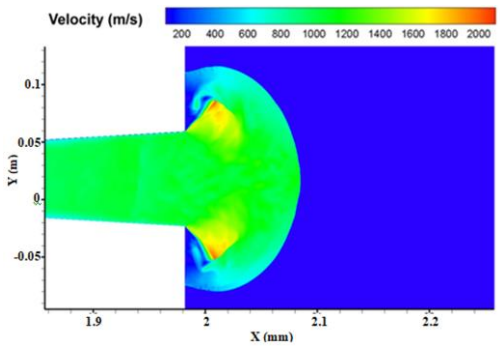

Fig. 14. Velocity mapping of the PDE exhaust plume.

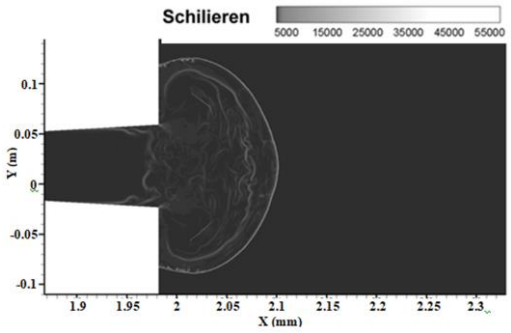

Fig. 15. Simulated Schlieren image of the PDE exhaust plume.

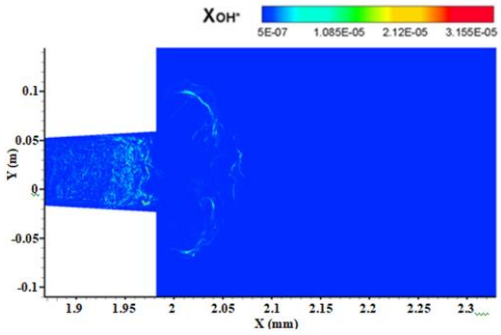

Fig. 16. Simulated OH* image of the PDE exhaust plume.

The detonation velocities' mapping shows that detonation is diffracted because the velocities in the plume were found mainly in the range of 700–1600 m/s. The Schlieren image allowed verifying that behind the shock front (~2.10 m at the centre) no reaction was present and fluctuations of density were observable of the spreading detonation. These fluctuations are in the same position (~2.07 m at the centre) of the reaction zone identified by the OH* image. The OH* image clearly demonstrates the diffraction of the detonation and a spread reaction zone. The detonation weakness was analogous to those reported by Gallier *et al.* (2017).

3.4 Evaluation of the Simulation Results

Some aspects of the simulation conditions probably had an effect on the simulation results. High pressure and temperature were required for the detonation initiation and propagation. The high refinement required due to the complexity of detonation phenomena was only established by high density changes because of the limitation of the commercial software applied. Usually, pressure and species concentration changes are also considered for increasing the cell number in the mesh refinement (Taylor *et al.*, 2013; Ettner *et al.*, 2014). These factors probably contributed to the high temperature simulated and to the diffraction of the detonation in its transmission into a larger volume.

However, the simulation results support some of the experimental observations (Lopes *et al*, 2019). The multi-headed detonation propagation characterized by simulated OH* images pointed out that the

detonation propagation is under a stable regime in the detonation tube. The experimental results showed overdriven detonation ca. 3% above CJ at the end of the detonation tube, the propagation was slightly decelerated in the expansion region (ca. 3.5% below CJ at the expansion entry) and the OH* images of the PDE exhaust plume reveal a multicellular detonation propagation in a stable regime (Lopes *et al*, 2019). As experimental results, the 2-D simulation coupled to a reduced chemical kinetics showed that detonation is decelerated in the expansion region (ca. 11% at the expansion entry), but it failed on how it was decelerated and predicted the diffraction of the detonation. A multi-headed detonation was expected in the whole engine, as experimental results demonstrated (Lopes *et al*, 2019).

Simulation studies with adaptive mesh refinement to resolve the cellular structure and a two-step chemistry model for the transmission from small channel to a larger area of a stable detonation with regular cellular pattern have shown decoupling of the reaction zone from the shock front and diffraction. A higher cell number than normal is required for stable detonation transmission (Jones *et al.*, 1996; Li *et al.*, 2016) and our simulated OH* images revealed a smaller number of cells immediately before detonation expanding through the nozzle, which could be related to the dilution effect at the interface of the two computational regions.

For detonation diagnostic purposes a 2-D simulation has recently been employed through a high-order WENO scheme with adaptive mesh refinement and explicit time integration with Runge–Kutta method for detailed chemical kinetics solution (Mével *et al.*, 2014; Gallier *et al.*, 2017), where the mass fractions were ensured to be positive with fifth-order accurate limitation (Gallier *et al.*, 2017). However, this work has shown that a 2-D simulation coupled to a reduced chemical kinetics with insertion of OH* reaction set could be able to follow the propagation dynamics of the H_2–air detonation through simulated OH* images.

Therefore, the detonation transmission into a larger volume, as the nozzle, probably requires higher refinement with additional parameters further to the density or a numerical method more accurate with high resolution such as WENO employed by non-commercial codes (He and Karagozian, 2006; Liu *et al.*, 2016; Mével *et al.*, 2014; Gallier *et al.*, 2017). Further, higher refinement or more accurate numerical method for simulations of the detonation propagation in the tube would need lower levels of pressure and temperature for initiation, which could eliminate the slight perturbations of the shock front verified by OH* images and maintain the detonation cell number until detonation expansion.

4. CONCLUSION

Two-dimensional CFD coupled to a reduced chemical kinetics simulation were carried out for an ideal hydrogen-fuelled PDE using a commercial code.
ZND calculations allowed proper selection of the reaction mechanism for 2-D CFD simulations with precision and low computational cost. The reduced reaction set tested and validated for several hydrogen combustion engines (rocket, PDE, RAM engines) was chosen and OH* chemical kinetics was added to it.

The two-dimensional CFD model coupled to a reduced chemical kinetics was validated through CJ parameters calculated by CEA and ZND codes, considering 10–15% of fluctuations acceptable. In spite of von Neumann pressures and temperatures being discrepant, probably due to the initiation method associated with the reaction mechanism applied, they did not significantly affect the detonation propagation and stabilization in the tube.

The insertion of the OH* chemical kinetics had little effect on the CJ parameters (<10%) and resulted in higher homogeneity with lower fluctuations of the detonation velocity field in the propagation front by the cylindrical tube of constant cross-section.

Furthermore, the addition of OH* to the reaction mechanism demonstrated clearly the detonation propagation regime through the cellular structure present as centres of high OH* concentration in the simulated images, which could be directly compared with the experimental data.

Simulated OH* images allowed verification of the stable regime of the stoichiometric H_2–air detonation with multicellular propagation by the whole tube and its diffraction through the nozzle accomplished by the velocity reduction of the wave front.

The simulation results confirm some of the experimental data, such as the stable detonation propagation by the tube and the velocity reduction in the expansion region. However, the applied 2-D simulation model was unsuccessful in predicting the PDE exhaust plume; the detonation transmission through an area changes it seemed to require more grid refinement or a more accurate numerical method.

Nevertheless, the inclusion of OH* chemical kinetics to a reduced reaction mechanism was enough to generate simulated OH* images for detonation front visualization that allows following appropriately the detonation propagation behaviour.

ACKNOWLEDGEMENTS

The authors thank Dr. Maurício Pinheiro Rosa and Dr. Lamartine N. Frutuoso Guimarães. This work was supported by the COMAER PROHIPER grant number IEAv-02/2015 – Hyper Project and CNPq grant number 471052/2012-4.

REFERENCES

Anetor, L., E. Osakue and C. Odetunde (2012). Reduced mechanism approach of modeling

premixed propane-air mixture using Ansys Fluent. *Engineering Journal* 16 (1), 67–86.

Benedick, W. B., C. M. Guirao, R. Knystautas and J. H. Lee (1986). Critical charge for the direct initiation of detonation in gaseous fuel-air mixtures, in Dynamics of explosion. J. C. Leyer, R. I. Soloukhin and J. R. Bowen, eds., *P*rogress in Astronautics and Aeronautcs Vol. 106, American Institute of Aeronautics and Astronautic, Reston, VI.

Boeck, L. R., F. M. Berger, J. Hasslberger and T. Sattelmayer (2016). Detonation propagation in hydrogen–air mixtures with transverse concentration gradients. *Shock and Waves* 26 (2), 181–192.

Boeck, L. R., F. M. Berger, J. Hasslberger, F. Ettner and T. Sattelmayer (2013). Macroscopic structure of fast deflagrations and detonations in hydrogen-air mixtures with concentration gradients. *In 24th International Colloquium on the Dynamics of Explosions and Reactive Systems (ICDERS)*, Taipei, Taiwan.

Bozhenkov, S. A., S. M. Starikovskaia and A. Yu Starikovskii (2003). Nanosecond gas discharge ignition of H_2^- and CH_4^- containing mixtures. *Combustion and Flame* 133 (1-2), 133-146.

Browne, S., Z. Liang and J. E. Shepherd (2005). Detailed and simplified chemical reaction mechanisms for detonation simulation. *In Fall Technical Meeting of the Western States Section of the Combustion Institute*, Stanford, CA, USA.

Debnath, P. and K. M. Pandey (2017). Numerical investigation of detonation combustion wave in pulse detonation combustor with ejector. *Journal of Applied Fluid Mechanics* 10 (2), 725-733.

Deiterding, R. and G. Bader (2005). High-resolution Simulation of Detonations with Detailed Chemistry, in G. Warnecke (Ed.), *Analysis and Numerics for Conservation Laws*, Springer, Berlin, Heidelberg Publishers.

Dupré, G., O. Péraldi, J. Joannon, J. H. Lee and R. Knystautas (1991). Limit criterion of detonation in circular tubes, in Dynamics of Detonations and Explosions: Detonations, In J. C. Leyer, A. A. Borisov, A. L. Kuhl, and W. A. Sirignano (Eds.), *Progress in Astronautics and Aeronautics* Vol. 133, American Institute of Aeronautics and Astronautic, Reston, VI.

Ebrahimi, H. B. and C. L. Merke (2002). Numerical simulation of a pulse detonation engine with hydrogen fuels. *Journal of Propulsion and Power* 18 (5), 1042-1048.

Eklund, D. and S. A. Stouffer (1994). A numerical and experimental study of a supersonic combustor employing sweep ramp fuel injectors. *In 30th Joint Propulsion Conference and Exhibit*, Indianapolis, IN, USA.

Ettner, F., K. G. Vollmer and T. Sattelmayer (2014). Numerical simulation of the deflagration-to-detonation transition in inhomogeneous mixtures. *Journal of Combustion* 1-15.

Fickett, W. and W. C. Davis (2010). *Detonation: Theory and Experiment*, 1. ed., Dover Publications, Mineola, NY.

Gallier, S., F. Le Palud, F. Pitgen, R. Mével and J. E. Shepherd (2017). Detonation wave diffraction in H2–O2–Ar mixtures. *Proceedngs of the Combustion Institute* 36 (2), 2781-2789.

Gamezo, V. N., D. Desbordes and E. S. Oran (1999). Formation and evolution of two-dimensional cellular detonations. *Combustion Flame* 116 (1–2), 154–165.

Gavrikov, A. I., A. A. Efimenko and S. B. Dorofeev (2000). A model for detonation cell size prediction from chemical kinetics. *Combustion and Flame* 120 (1–2), 19–33.

He, X. and A. R. Karagozian (2006). Pulse-detonation-engine simulations with alternative geometries and reaction kinetics. *Journal of Propulsion and Power* 22 (4), 852–861.

Im, K. S. and S. T. J. Yu (2003). Analyses of direct detonation initiation with realistic finite-rate chemistry. *In 41th Aerospace Sciences Meeting & Exhibit*, Reno, NV, USA.

Ivanov, M. F., A. D. Kiverin and M. A. Liberman (2011). Flame acceleration and DDT of hydrogen-oxygen gaseous mixtures in channels with no-slip walls. *International Journal of Hydrogen Energy* 36 (13), 7714–7727.

Jones, D. A., G. Kemister, E. S. Oran and S. Michel (1996). The influence of the cellular structure on detonation transmission. *Shock and Waves* 6, 119-129.

Kailasanath, K. (2000). Review of propulsion applications of detonation waves. *AIAA Journal* 38 (9), 1698–1708.

Kailasanath, K. and D. A. Schwer (2017). High-fidelity simulations of pressure-gain combustion devices based on detonations. *Journal of Propulsion and Power* 33 (1), 153-162.

Kao, S. and J. E. shepherd (2008). Numerical solution methods for control volume explosions and ZND detonation structure. *Technical Report FM2006.007*, Aeronautics and Mechanical Engineering, California Institute of Technology, California, USA.

Kathrotia, T., M. Fikri, M. Bozkurt, M. Hartmann, U. Riedel and C. Schulz (2010). Study of the H+O+M reaction forming OH*: Kinetics of OH* chemiluminescence in hydrogen combustion systems. *Combustion and Flame* 157 (7), 1261–1273.

Kim, H., F. K. Lu, D. A. Anderson and D. R. Wilson (2003). Numerical simulation of detonation process in a tube. *Computational*

Fluid Dynamics Journal 12 (2), 227-241.

Lee, J. (2008). *The Detonation Phenomenon*, 1. ed., Cambridge University Press, New York, NY.

Li, J., J. G. Ning, C. B. Kiyanda and H. D. Ng (2016). Numerical simulations of cellular detonation diffraction in a stable gaseous mixture. *Propulsion and Power Research* 5 (3), 177-183.

Liu, Y., W. Zhang and Z. Jiang (2016). Relationship between ignition delay time and cell size of H2-Air detonation. *International Journal of Hydrogen Energy* 41 (28), 11900–11908.

Lopes N. C., C. C. B. Katata and C. S. T. Marques (2019). Diagnostic method based on spontaneous emission for pulse detonation engines. *Experimental Thermal and Fluid Science* 102, 261-270.

Maciel, E. C. (2017). *Estudo numérico de um motor de detonação pulsada*, MSc Thesis, Instituto Tecnológico de Aeronáutica, São José dos Campos, Brasil.

Magnussen, B. J. (2005). The eddy-dissipation concept a bridge between science and technology. *In ECCOMAS Thematic Conference on Computational Combustion*, Lisbon, Portugal.

Marques, C. S. T., A. C. Oliveira, F. Dovichi Filho, W.C. Ferraz and J. B. Chanes Jr. (2010). Single-shot pulsed detonation device for PDE combustion simulation. *In 13th Brazilian Congress of Thermal Science and Enginering*, Uberlândia, MG, Brasil.

Mehta, U. B. (1998). Credible computational fluid dynamics simulations. *AIAA Journal* 36 (5), 665–667.

Mével, R. (2009). *Étude de mécanismes cinétiques et des propriétés. explosives des systèmes hydrogène-protoxyde d'azote et silane-protoxyde d'azote. Application à la securité industrielle*, Ph.D Thesis, Université d'Orléans, Orléans, France.

Mével, R., D. Davidenko, F. Lafosse, N. Chaumeix, G. Dupré, C. E. Paillard and J. E. Shepherd (2015). Detonation in hydrogen–nitrous oxide–diluent mixtures: an experimental and numerical study. *Combustion and Flame* 162 (5), 1638-1649.

Mével, R., D. Davidenko, J. M. Austin, F. Pitgen and J. E. Shepherd (2014). Application of a laser induced fluorescence model to the numerical simulation of detonation waves in hydrogen-oxygen- diluent mixtures. *International Journal of Hydrogen Energy* 39 (11), 6044–6060.

Navaz, H. K. and R. M. Berg (1998). Numerical treatment of multi-phase flow equations with chemistry and stiff source terms. *Aerospace Science and Technology* 2 (3), 219–229.

Nicholls, J. A., H. R. Wilkinson, R. B. Morrison (1957). Intermittent Detonation as a Thrust-Producing Mechanism. *Journal of Jet Propulsion* 27, 534–541.

Perkins, H. D. and C. J. Sung (2005). Effects of fuel distribution on detonation tube performance, *Journal of Propulsion and Power* 21 (3), 539-545.

Petersen, E. L. and R. K. Hanson (1999). Reduced kinetics mechanisms for ram accelerator combustion. *Journal of Propulsion and Power* 15 (4), 591–600.

Pitgen, F., C. A. Eckett, J. M. Austin and J. E. Shepherd (2003). Direct observations of reaction zone structure in propagating detonations. *Combustion and Flame* 133 (3), 211–229.

Powers, J. M. and S. Paolucci (2005). Accurate spatial resolution estimates for reactive supersonic flow with detailed chemistry. *AIAA Journal* 43 (5), 1088–1099.

Rankin, B. A., D. R. Richardson, A. W. Caswell, A. G. Naples, J. L. Hoke and F. R. Schauer (2017). Chemiluminescence imaging of an optically accessible non-premixed rotating detonation engine. *Combustion and Flame* 176, 12–22.

Rodrigues, V. B., E. C. Maciel and C. S. T. Marques (2015). H_2-air chemical kinetic evaluation for pulse detonation engine simulations. *In Australian Combustion Symposium*, Melbourne, VIC, Australian.

Rudy, W., A. Dabkowski and A. Teodorczyk (2014). Experimental and numerical study on spontaneous ignition of hydrogen and hydrogen-methane jets in air. *International Journal of Hydrogen Energy* 39 (35) (2014), 20388–20395.

Smirnov, N. N. and V. F. Nikitin (2014). Modeling and simulation of hydrogen combustion in engines. *International Journal of Hydrogen Energy* 39 (2), 1122–1136.

Srihari, P., P., M. A. Mallesh, G. Sai Krishna Prasad, B. V. N. Charyulu and D. N. Reddy (2015). Numerical study of pulse detonation engine with one-step overall reaction model. *Defence Science Journal* 65 (4), 265–271.

Stoddard, W., R. Driscoll and E. J. Gutmark (2011). Comparative numerical and experimental study of pulse detonation initiation through crossover shock. *In 49th AIAA Aerospace Sciences Meeting including the New Horizons Forum and Aerospace Exposition*, Orlando, FL, USA.

Sugiyama, Y. and A. Matsuo (2012). Numerical investigation on the detonation regime with longitudinal pulsation in circular and square tubes. *Combustion and Flame* 159 (12), 3646–3651.

Tangirala, V., B. Varatharajan and A. J. Dean

(2003). Numerical investigations of direct initiation of detonations in hydrocarbon fuel/air mixtures. *In 41st Aerospace Sciences Meeting and Exhibit*, Reno, NV, USA.

Taylor, B. D., D. A. Kessler, V. N. Gamezo and E. S. Oran (2012). The influence of chemical kinetics on the structure of hydrogen-air detonations. *In 50th AIAA Aerospace Sciences Meeting including the New Horizons Forum and Aerospace Exposition*, Nashville, TN, USA.

Taylor, B. D., D. A. Kessler, V. N. Gamezo and E. S. Oran (2013). Numerical simulations of hydrogen detonations with detailed chemical kinetics. *Proceedings of the Combustion Institute* 34 (2), 2009–2016.

Thomas, G. O. (2009). Flame acceleration and the development of detonation in fuel-oxygen mixtures at elevated temperatures and pressures. *Journal Hazardous Materials* 163 (2–3), 783–794.

Virot, F., B. Khasainov, D. Desbordes and H. N. Presles (2009). Operating limit of a pulsed detonation engine. The marginal case of detonation propagation. *In 47th AIAA Aerospace Sciences Meeting including the New Horizons Forum and Aerospace Exposition*, Orlando, FL, USA.

Wolański, P. (2013) Detonative propulsion. *Proceedings of the Combustion Institute* 34 (1), 125–158.

Wu, Y., F. Ma and V. Yang (2003). System performance and thermodynamic cycle analysis of airbreathing pulse detonation engine. *Journal of Propulsion and Power* 19 (4), 556–567.

Yi, T. H., F. K. Lu, D. R. Wilson and G. Emanuel (2017). Numerical study of detonation wave propagation in a confined supersonic flow. *Shock and Waves* 27 (3), 395-408.

Yungster, S., K. Radhakrishnan and K. Breisacher (2006). Computational study of NOx formation in hydrogen-fuelled pulse detonation engines. *Combustion Theory and Modelling* 10 (6), 981-1002.

Zhang, Z., Z. Li, Y. Wu and X. Bao (2016). Numerical studies of multi-cycle detonation induced by shock focusing. *In ASME Turbo Expo 2016: Turbomachinery Technical Conference and Exposition*, Seoul, South Korea.

Zhukov, V. P. (2012). Verification , validation and testing of kinetic models of hydrogen combustion in fluid dynamic computations. *ISRN Mechanical Engineering* 2012 (475607), 1-11.